Progress in Earth and Planetary Science

RESEARCH ARTICLE Open Access

Mineralogical and physico-chemical properties of halloysite-bearing slip surface material from a landslide during the 2018 Eastern Iburi earthquake, Hokkaido

Jun Kameda

Abstract

Destructive landslides were triggered by the 6.7 M_w Eastern Iburi earthquake that struck southern Hokkaido, Japan, on 6 September 2018. Heavy rainfall on 4 September in addition to intermittent rainfall around the Iburi Tobu area saturated and weakened the slope-forming materials (mostly altered volcanoclastic soils), making them susceptible to failure because of the earthquake's strong ground motion. Most of the shallow landslides exhibited long runouts along gentle hill slopes, with characteristic halloysite-bearing slip surface at the base of the volcanic soils. This study investigated the mineralogical and physico-chemical properties of the slip surface material with the aim of understanding weakening and post-failure behaviors during the landslides. Halloysite in the slip surface had irregular-to-hollow-spherical morphology with higher mesopore volumes than tubular halloysite, which is related to a high capacity for water retention after rainfall. To reproduce possible chemical changes in the slip surface during rainfall, the sample was immersed in varying amounts of rainwater; solution pH increased and ionic strength decreased with increasing water content. These findings, alongside electrophoretic analysis, suggest that rainwater infiltration could have increased the absolute zeta potential value of the slip surface material. It is suggested that rainfall before the earthquake enhanced the colloidal stability of halloysite particles within the slip surface, owing to an increase in electrostatic repulsion. This decreased the material's cohesive strength, which might have led to destabilization of the slope during ground shaking generated by the earthquake, and subsequent high-mobility flow after failure.

Keywords: 2018 Hokkaido Eastern Iburi earthquake, Shallow landslide, Liquefaction, Halloysite

1 Introduction

The Eastern Iburi earthquake (M_w = 6.7) occurred at 3:07 AM (local time) on 6 September 2018 in southern Hokkaido, Japan (Fig. 1a). The resulting strong ground motion (with a maximum intensity of 7 on the Japan Meteorology Agency [JMA] intensity scale) caused hill slopes near the epicenter to fail suddenly. These slopes are widely covered by volcanic soils that originated from nearby volcanoes such as Tarumai, Eniwa, and Shikotsu (Yamada 1958; Katsui 1959; Furukawa and Nakagawa 2000). Around 6000 landslides occurred in the area (Yamagishi and Yamazaki 2018), with many of the recorded landslides being shallow and exhibiting features of liquefaction, such as long runouts of debris on relatively gentle slopes (< ~ 30°; Osanai et al. 2019; Kasai and Yamada 2019). Field surveys revealed that the basal part of the volcanic soils acted as the principal slip surface (Chigira et al. 2019; Kameda et al. 2019; Ito et al. 2020); most of these soils characteristically contain the mineral halloysite (Chigira et al. 2019; Kameda et al. 2019).

Halloysite is a typical alteration product in pyroclastic deposits and generally occurs after allophane in the

Correspondence: kameda@sci.hokudai.ac.jp
Department of Earth and Planetary Sciences, Faculty of Science, Hokkaido University, 10W8, Kita-ku, Sapporo 060-0810, Japan

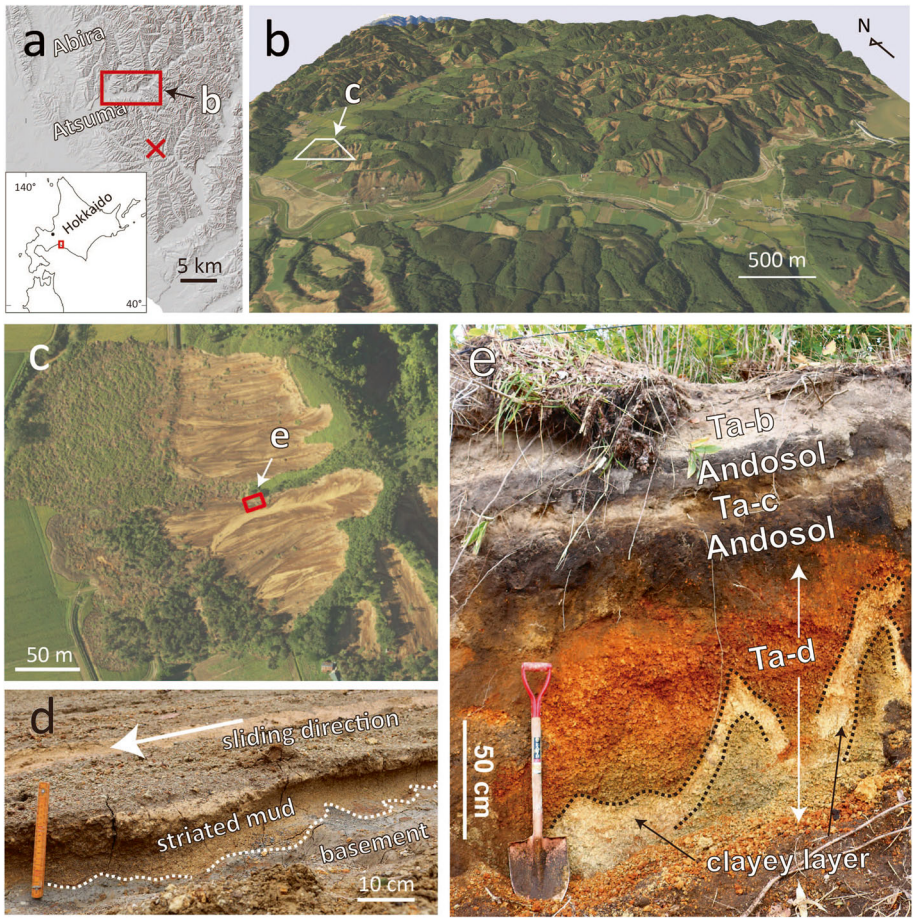

Fig. 1 Location and occurrence of the studied landslide. (a) Locations of the epicenter of the Eastern Iburi earthquake (red cross) and the study area. (b) 3D view of the hills near Atsuma after the earthquake (produced by data from the Geospatial Information Authority of Japan 2018a). (c) Close-up photograph of the studied landslide (taken on 6 September 2018; Geospatial Information Authority of Japan 2018b). (d) Striated mud on the collapsed slope (modified after Kameda et al. 2019). (e) Scarp measuring 2–3 m in height, which contains a stratigraphic sequence of volcanoclastic deposits (modified after Kameda et al. 2019). The slip surface material analyzed in this study was collected where the "clay layer" is in contact with the basement Neogene marine strata.

weathering sequence (Wada 1977, 1980; Parfitt et al. 1983). Halloysite exhibits various morphologies in nature; the most common form is elongated tubes, but spheroidal and platy halloysite has also been observed (Askenasy et al. 1973; Joussein et al. 2005). Halloysite often occurs on the slip surface of landslides in volcanic areas of Japan (Chigira and Yokoyama 2005; Chigira et al. 2012), Indonesia (Nakano et al. 2013), and New Zealand (Moon 2016; Kluger et al. 2017). Spherical halloysite is most common in such cases (Smalley et al. 1980). In general, halloysite-bearing soils and deposits exhibit higher peak as well as residual friction angles than those that contain platy clay minerals, which suggests that they may be stable on steep slopes (Moon 2016). However, the material also exhibits high sensitivity (i.e., loss of strength by remolding), which possibly causes high-mobility flows after failure (Moon 2016). Moon (2016) also suggested the important effects of physico-chemical interactions between the clay surfaces and cations in pore water on the rheological properties of halloysite-bearing soils. Rheological experiments have demonstrated that the flow properties of halloysite suspensions depend on the solution chemistry (pH and NaCl concentration), which modify the halloysite surface properties and influence the resulting association types of individual particles (Theng and Wells 1995). Recently, Kluger et al. (2017) observed halloysite with a unique morphology in a tephra layer involved in a flow slide and suggested that weak interparticle interactions contributed to the high sensitivity of the material. These findings indicate that evaluation of the surface physico-chemical properties of the constituent halloysite mineral and their changes in response to contacting pore water is key to understanding the mechanism of landslide initiation, as well as their runout behavior in volcanic areas. This study analyzed the mineralogical and physico-

chemical properties of the slip surface material from a landslide triggered by the Eastern Iburi earthquake, and used the results to discuss the possible weakening process of the material and the factors that caused the subsequent slope failure.

2 Studied landslide

The studied landslide is located in the Tomisato district of Atsuma town, southern Hokkaido (Fig. 1a, b). The hill had a slope of ~ 20°, dipping westward; the hill largely collapsed, and slid downward with a runout distance of ~ 100 m (Fig. 1c). The collapsed slope was covered by clayey striated mud (Fig. 1d), which was often wet during field surveys. The scarp of the landslide exhibited a stratigraphic sequence of pyroclastic deposits supplied from the Tarumai Volcano on a basement of Neogene marine beds: Ta-b (AD1667; Nakagawa et al. 2018), Ta-c (ca. 2.5 ka), and Ta-d (ca. 9 ka) deposits with two interbedded andosol layers (Fig. 1e). A clayey layer (argillized pumice), several tens of centimeters thick and resembling the striated mud on the slope, was observed at the base of the scarp within the Ta-d deposit. The characteristic undulating appearance of the clay layer is assumed to be related to soil liquefaction during strong coseismic shaking (Kameda et al. 2019). Based on field observations as well as the results of laboratory measurements, the clayey layer was in most cases found to act as a slip surface during the landslide. X-ray diffraction analysis revealed that the slip surface principally contained halloysite (Kameda et al. 2019). The volcanic soils including the slip surface material may be soaked and weakened by heavy rainfall due to a typhoon on 4 September and intermittent rainfall over several weeks before the Eastern Iburi earthquake (Fig. 2). Surveys of several other locations indicated that many of the shallow landslides around this area show similar geological background and that they were triggered by the earthquake in a similar manner (Kameda et al. 2019; Wang et al. 2019; Zhang et al. 2019; Ito et al. 2020).

3 Methods

3.1 X-ray diffraction (XRD) analysis

Previous XRD analysis of the clay-size fraction of the slip surface material has revealed the occurrence of halloysite (Kameda et al. 2019). This study additionally conducted bulk XRD to quantify the halloysite content. The bulk powder sample, mixed with corundum (AX-5H, Hinomoto Kenmazai Co.) as an internal standard at a weight ratio of 4:1, was mounted on a glass holder by side loading to minimize the development of a preferred alignment of the clay minerals. XRD patterns were recorded using a MAC Science MX-Labo with monochromatized CuKα radiation at 40 kV and 30 mA, 1° divergence and anti-scattering slits, and a 0.15 mm receiving slit in continuous scan mode at a rate of 1° 2θ per minute. The weight contents of crystalline phases such as halloysite and other minerals were determined using the reference intensity ratio (RIR) (Hillier 2000). The RIR value I/I_{cor} of the halloysite peak at ~ 20° (d = 4.4 Å), relative to corundum, was determined to be 0.225 from the measurement of a 50:50 mixture using a commercially available reference sample (Halloysite nanoclay, Sigma-Aldrich). The halloysite peak at ~ 20° (020 110 composite reflection) was chosen for this analysis because it is

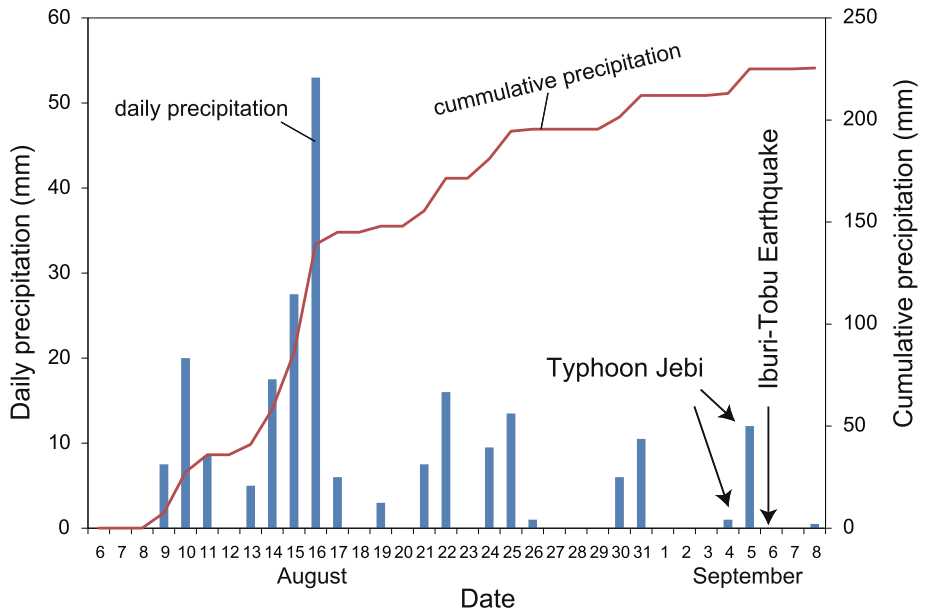

Fig. 2 Daily and cumulative precipitations observed at the Atsuma station (Japan Meteorological Agency)

believed to be less affected by changes in interlayer spacing and preferential alignment of particles than the 00*l* basal reflection (Środoń et al. 2001). The reference halloysite sample was a synthetic powder with tubular morphology (50 nm outer diameter and 15 nm inner diameter; https://www.sigmaaldrich.com/). In the following, the reference sample was not further purified before use.

3.2 Transmission electron microscopy (TEM) observation

The morphological features of the halloysite-bearing slip surface material were observed by TEM under vacuum (JEM-2100F, Jeol). For TEM observation, the fine fraction of the sample was separated by centrifugation and dispersed on a holey carbon film.

3.3 Specific surface area and pore size distribution by N_2 adsorption–desorption analysis

The specific surface area and pore size distribution (PSD) of the samples were measured using an automated sorption analyser (Autosorb, Quantachrome Instruments). Prior to measurement, the samples were dried and degassed at 105 °C for 15 h under vacuum. This treatment potentially causes dehydration of the interlayer water, which in turn may change the diameter of individual halloysite particles by ~ 10–20% (Joussein et al. 2005). Nitrogen adsorption–desorption assessed at 77 K provided isotherms for Brunauer–Emmett–Teller (BET) analysis to determine the surface areas. The adsorption isotherm was also provided for PSD analysis based on the Barrett–Joyner–Halenda (BJH) method (Barrett et al. 1951). For comparison, we also analyzed the reference samples of halloysite and allophane (Sekado-2, Shinagawa General Co., Ltd.). The reference allophane was a purified sample collected from Kitakami pumice, Iwate, Japan. The allophane particles has a hollow spherical morphology with ~ 5 nm outer diameter and ~ 3 nm inner diameter (Brigatti et al. 2006).

3.4 Water adsorption–desorption measurement

The adsorption and desorption of water were measured using an automated sorption analyser (N-VP, Microtrac-BEL). Prior to measurement, the bulk powder sample was dried and degassed at 105 °C for 15 h under vacuum. The water adsorption–desorption isotherm was obtained at 25 °C for relative pressures, P/P_0, ranging from 0 to 0.9.

3.5 Immersion of the slip surface material in distilled water and rainwater

To simulate possible changes of the solution chemistry of pore water within the slip surface during rainfall, dried bulk samples were immersed in rainwater and distilled water (FUJIFILM Wako Pure Chemicals Co.) at different solid/water weight ratios (S/W) for 24 h. The resulting solutions were separated by filtering the mixtures through a 0.45 μm filter attached to the tip of a syringe, and their pH and electrical conductivity (EC) were measured. The rainwater was sampled on 30 August 2020 at Atsuma town in the same season as when the disaster occurred. Before the experiments, solid contaminants were removed from the rainwater by using the 0.45 μm filter.

3.6 Zeta potential and dynamic light scattering analysis

For electrophoretic measurement, samples were centrifuged to separate the > 2 μm clay fraction. Samples were then dialyzed using distilled water until the conductivity of the outside solution became ~ 2.0 μS/cm. The electrophoretic mobility μ of the sample was measured using a Zetasizer Nano (Malvern), and the zeta potential ζ was obtained as follows based on the Smoluchowski relationship (Smoluchowski 1921):

$$\mu = \frac{\varepsilon_0 \varepsilon \zeta}{\eta}, \tag{1}$$

where ε_0 is the vacuum permittivity, ε is the dielectric constant of water, and η is the viscosity of the solution. The pH of the solution was adjusted by adding HCl and NaOH (0.01 N) solutions with background ionic strength of 10^{-2}, 10^{-3}, and 10^{-4} M NaCl.

The hydrodynamic diameter of the particles (spherical equivalent) was measured using the same apparatus as that used for electrophoretic mobility measurement (Zetasizer Nano), which used dynamic light scattering after 24 h of the sample being immersed in solutions of different ionic strengths (10^{-4}–0.5 M NaCl).

4 Results and discussion

Figure 3 shows the XRD pattern of the slip surface material with a corundum internal standard. The pattern shows peaks for halloysite, plagioclase, and clinopyroxene. The RIR method yielded halloysite, plagioclase, and clinopyroxene contents of ~ 40%, ~ 4%, and ~ 4%, respectively, with the remainder (~ 50%) being amorphous low-crystalline materials such as volcanic glass and possibly allophane.

The TEM observation revealed that halloysite in the slip surface was mostly irregularly shaped, but some particles appeared as hollow spheres with a wall thickness of several tens of nanometers (Fig. 4). The particles often formed large aggregates several hundreds of nanometers in diameter. Tubular halloysite was rarely observed.

Figure 5a shows the N_2 adsorption–desorption isotherms of the three samples; Table 1 summarizes the specific surface area and total pore volume determined from these isotherms. The total pore volumes, estimated

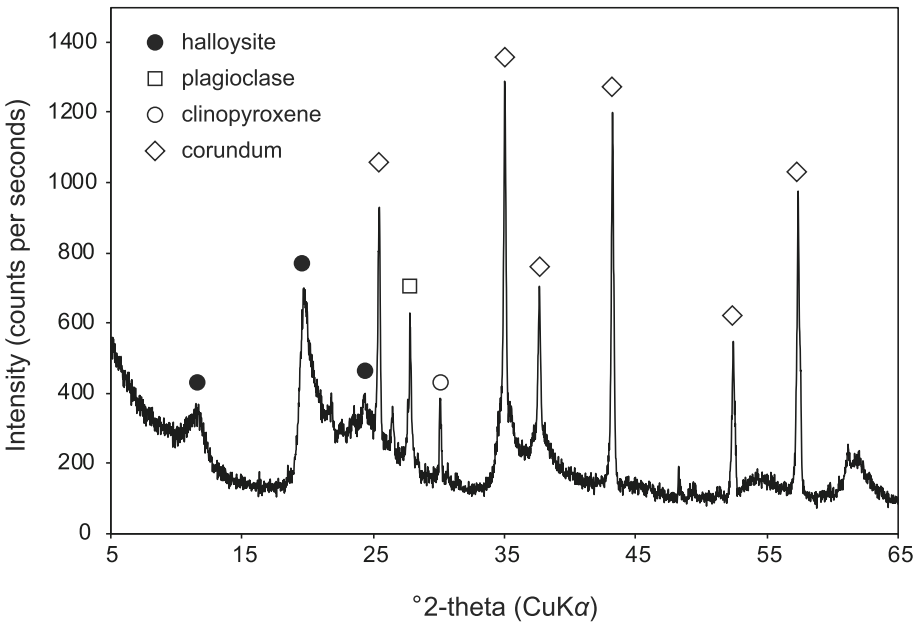

Fig. 3 Bulk XRD pattern of the slip surface material with a corundum internal standard

from the amounts of adsorbed N_2 at a relative pressure of P/P_0 = 0.99, are almost the same for the three samples (0.35–0.39 m^3/g). The specific surface areas of the reference halloysite and allophane are 49 and 285 m^2/g, respectively, consistent with previous results for the same samples (Saeki et al. 2010; Em et al. 2020), whereas the slip surface material exhibited an intermediate value between the two reference samples (118 m^2/g). It should be noted, however, that these values include uncertainty due to the change in the dimensions of the halloysite particles during the pretreatment for the adsorption measurement. The reference halloysite showed a

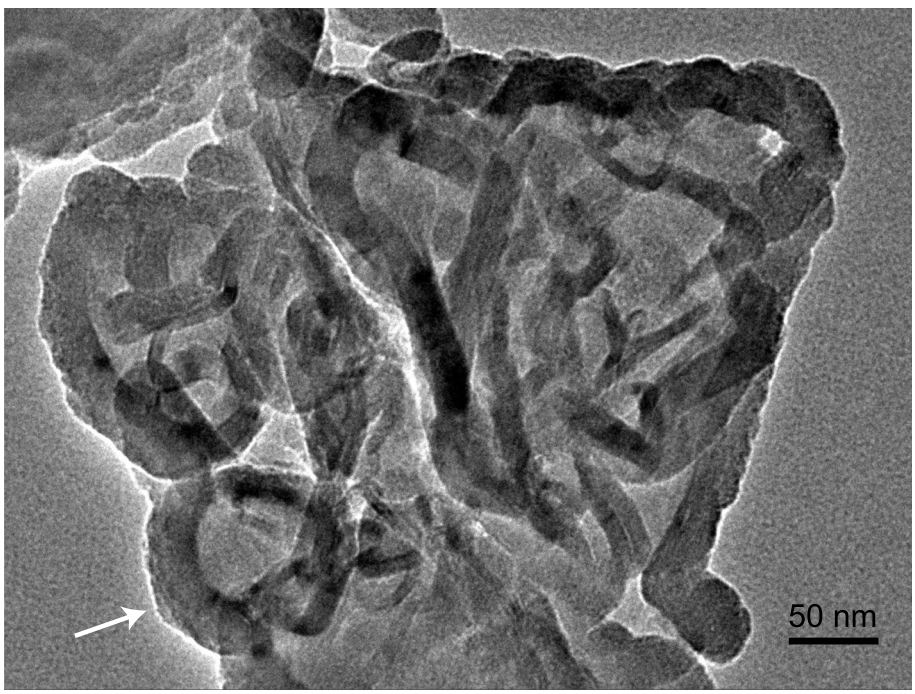

Fig. 4 TEM micrograph of halloysite in the slip surface. The particle indicated by the arrow is a hollow sphere

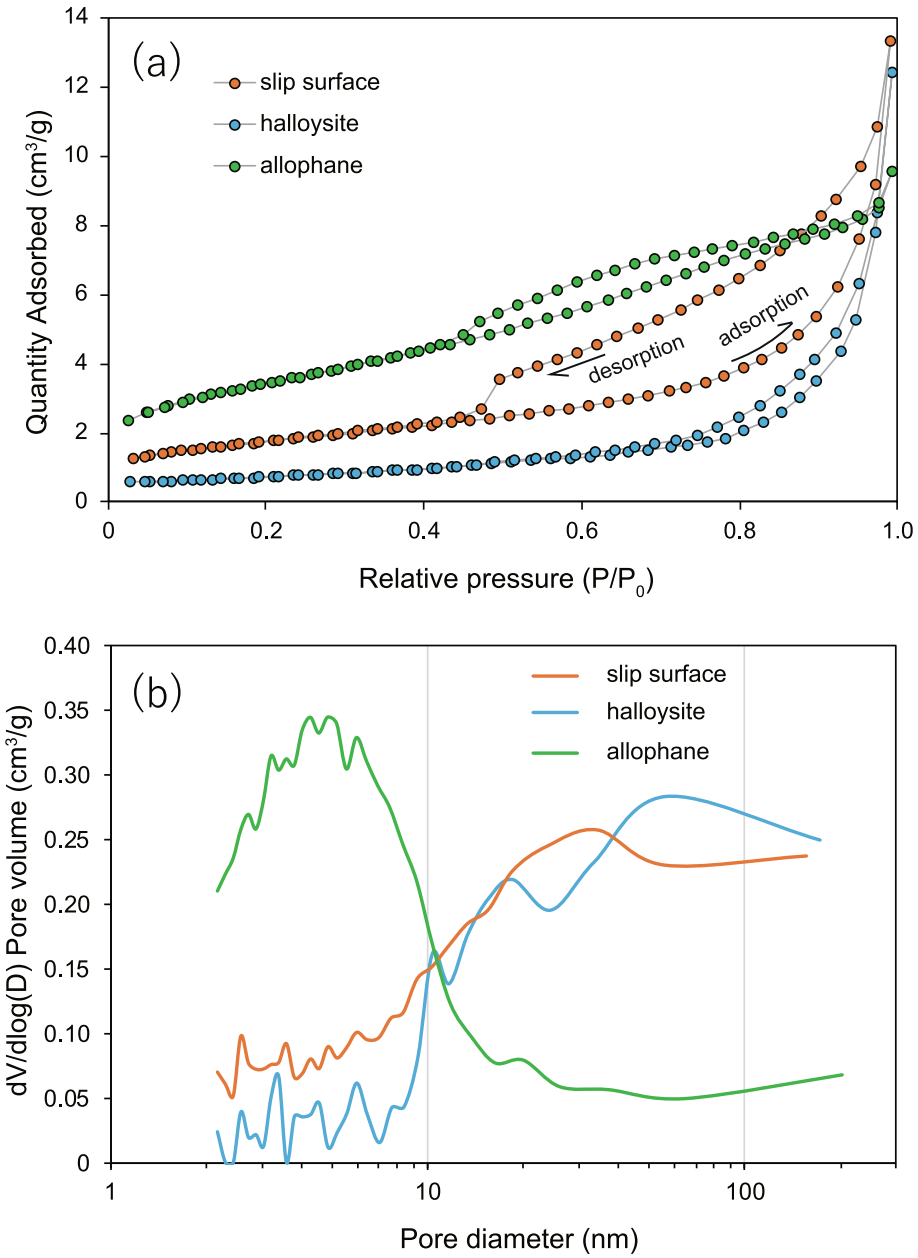

Fig. 5 Results of the N_2 adsorption–desorption experiments. (a) N_2 adsorption–desorption isotherms for the slip surface material, halloysite, and allophane. (b) Pore size distribution (PSD) curves obtained from BJH analysis

reversible Type II isotherm from the classification of The International Union of Pure and Applied Chemistry (IUPAC) (Sing et al. 1985), suggesting that the sample contained predominantly macropores (> 50 nm), which is also supported by the PSD curve derived from the BJH method (Fig. 5b). The reference allophane exhibited a type IV isotherm with some hysteresis indicating the presence of mesopores (Iyoda et al. 2012). The PSD indicates the occurrence of mesopores with a peak around 4–5 nm in size, possibly corresponding to the

Table 1 Specific surface area and total pore volume of the slip surface material, standard halloysite, and allophane

	Slip surface material	Halloysite	Allophane
Specific surface area (m^2/g)	118	49	285
Total pore volume (cm^3/g)	0.394	0.361	0.348

interparticle and inter-microaggregate spaces of allophane particles (Wang et al. 2020). Micropores (< 2 nm) due to the crust of allophane particles may also have contributed to the increased amounts of adsorbed N_2 compared with the other samples (Wada 1989; Tomura et al. 1997). The adsorption isotherm of the slip surface material resembles that of the reference halloysite but shows a clear hysteresis loop indicating the presence of mesopores. The PSD shows higher volumes of mesopores (ranging from ~ 2 to 40 nm) than the reference halloysite.

Figure 6 shows water adsorption–desorption isotherms of the three samples. Allophane showed the greatest water adsorbed with two step rises of the isotherm at P/P_0 = 0–0.3 and 0.6–0.9; these are possibly attributable to capillary condensation of water at micropores and mesopores, respectively (Tomura et al. 1997; Suzuki et al. 2001). Such a step-like rise was not shown by the slip surface material or the reference halloysite. The adsorbed amounts of water on the slip surface material were approximately twice as large as those of the reference halloysite.

Figure 7 shows the results of immersion tests. The pH of the rainwater increased as the amount of water used for immersion increased, rising from ~ 6.3 at S/W = 0.65 to ~ 7.0 at S/W = 0.2. In contrast, the EC of the solution decreased as the amount of water increased, from 60 μS/cm at S/W = 0.65 to 30 μS/cm at S/W = 0.2. These values correspond to ~ 5.0×10^{-4} and ~ 0.25×10^{-4} M NaCl, respectively (from the table of International Electrotechnical Commission IEC 60746-3). Using distilled water obtained almost similar results (Fig. 7).

Figure 8 shows the results of electrophoretic analysis of the slip surface material. For comparison, reference allophane and halloysite were also analyzed (Fig. 8a). The zeta potential of allophane increased from − 35 mV at pH = ~ 12 to + 30 mV at pH = ~ 2, with a point of zero charge (PZC) at pH = ~ 6. The zeta potential of the reference halloysite increased from − 45 mV at pH = ~ 10 to + 10 mV at pH = ~ 2, with a PZC at pH = ~ 3. These results are largely consistent with the literature (Vergaro et al. 2010; Kawachi et al. 2013). The zeta potential of the slip surface material largely behaved in a similar manner to the reference halloysite but differed at lower pH. We also examined the dependence of ionic strength on the zeta potential of the slip surface material. Figure 8b indicates that the zeta potential decreased (an increase in absolute value) as ionic strength decreased from 10^{-2} to 10^{-4} M particularly at pH > 3.5.

The hydrodynamic diameter of the particles was ~ 1000 nm below 5.0×10^{-4} M NaCl (Fig. 9). It initially increased up to 3000 nm as ionic strength increased, then dropped to ~ 2000 nm at < 0.05 M.

The studied landslide was eventually triggered by the earthquake, but heavy rainfall due to a typhoon and intermittent rainfall over several weeks before the earthquake saturated and weakened the volcanic soil on the slope (Fig. 2). The slip surface at the base of the volcanic soil characteristically contains water-absorbent halloysite, thus it may have been wet for a long period after rainfall, as was observed by Kameda et al. (2019).

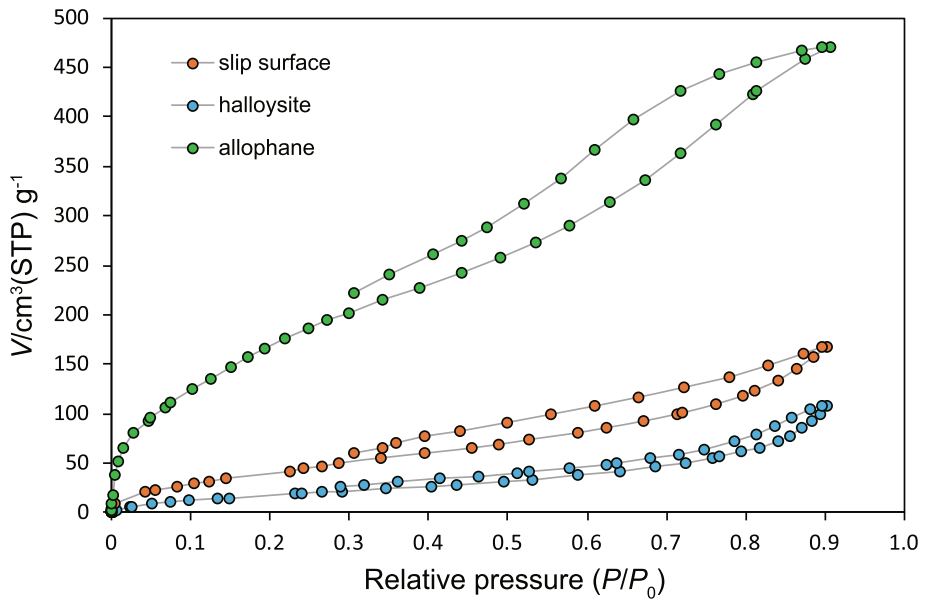

Fig. 6 Water adsorption–desorption isotherms at 25 °C for the slip surface material, halloysite, and allophane

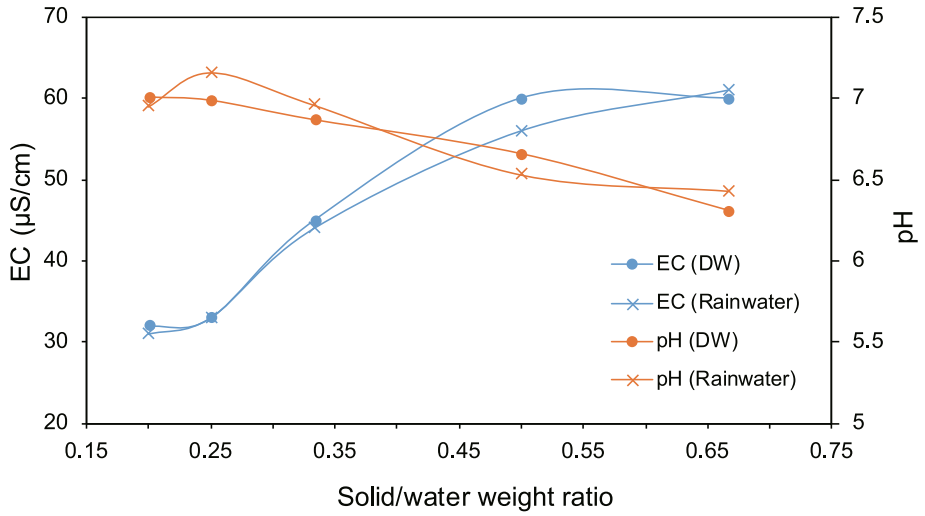

Fig. 7 Results of immersion tests. Changes in pH and electrical conductivity after sample immersion for 24 h in rainwater or distilled water (DW) at different solid/water weight ratios

According to Noro et al. (1981) and Noro (1986), the rate of dehydration of halloysite depends on the morphological features and generally decreases in the order: long tubular halloysite > platy halloysite > spheroidal halloysite. Halloysite in the slip surface had an irregular-to-hollow-spherical morphology, which may also have contributed to its high water retention capacity. The present adsorption experiment demonstrated that the slip surface material has larger mesopore volumes than the tubular halloysite, as represented by a larger hysteresis loop (Figs. 5 and 6), possibly due to peculiar morphological features of the halloysite or the presence of allophane (Fig. 4). However, Wada and Mizota (1979) found that halloysite in the Ta-d layer (i.e., strata identical to the slip surface) comprised particles shaped like wood shavings. Other researchers reported the presence of platy halloysite particles based on the TEM observation on the samples taken from the sliding surfaces of some landslides triggered by the same earthquake (Earthquake and Volcano Hazards Observation and Research Program 2019). Therefore, the morphological features of halloysite possibly depend on location, even within a given stratum.

The immersion test results suggest that successive rainwater infiltration of the slip surface could have modified the pore water chemistry, with pH increasing and ionic strength decreasing (Fig. 7). The zeta potential measurements (Fig. 8) suggest that both these changes enhanced the stability of colloidal halloysite particles as the absolute values of zeta potential increased. This implies a qualitative decrease in the soil's cohesive strength (Plaza et al. 2018).

Applying the classic theory of Derjaguin–Landau–Verwey–Overbeeck (DLVO theory) for colloidal stability, I attempted to estimate the interparticle potential of the halloysite particles. The potential energy can be obtained by the sum of the electrostatic double layer (i.e., repulsive energy V^{EL}) and Lifshitz–van der Waals (attractive energy V^{LW}) interactions as a function of distance between the particles s:

$$V_T = V^{EL}(s) + V^{LW}(s). \tag{2}$$

For spherical particles, these energies can be expressed as follows (Duran et al. 1998; Israelachvili 2011):

$$V^{EL}(s) = 2\pi\varepsilon_0\varepsilon a\zeta^2 \ \ln\left(1 + \ exp(-\kappa s)\right), \tag{3}$$

$$V^{LW}(s) = -\frac{A}{6}\left(\frac{2a^2}{s(4a+s)} + \frac{2a^2}{(2a+s)^2} + \ln\left(\frac{s(4a+s)}{(2a+s)^2}\right)\right), \tag{4}$$

where a is the particle radius, A is the Hamaker constant, and κ is the reciprocal of the Debye length (double-layer thickness). Applying a = 1000 nm from the dynamic light scattering experiment (Fig. 9) and A = 2.5×10^{-20} J (a silicate surface typically shows A = ~ (1–5) × 10^{-20} J; Lagaly 2006), the interparticle potentials (in kT where k is the Boltzmann constant and T is temperature in kelvin) can be plotted as in Fig. 10.

The interparticle potential increased as ionic strength decreased at constant zeta potential (− 35 mV; Fig. 10a). For a constant ionic strength, the interparticle potential increased as the zeta potential decreased (an increase in absolute value; Fig. 10b). These results also suggest that increasing pH and decreasing ionic strength due to increasing rainwater infiltration enhanced the interparticle

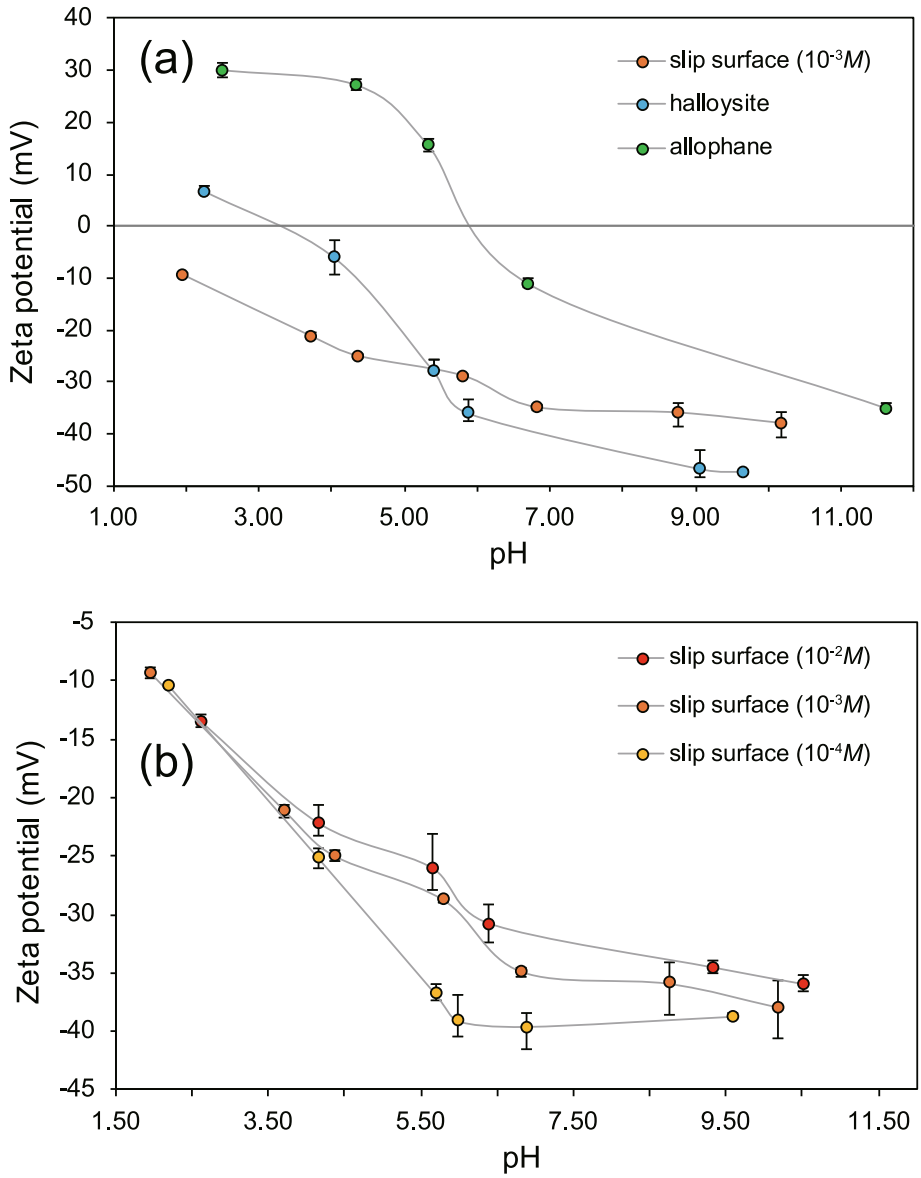

Fig. 8 Results of electrophoretic analysis. (a) Zeta potentials with respect to pH. Results for reference halloysite and allophane samples are included for comparison. (b) Zeta potentials with respect to pH at different solute concentrations. Error bars denote the range of three repeated measurements

potential, thereby causing a loss in cohesive strength of the material. Kameda et al. (2019) reported that natural water content during a field survey was ~ 150%, which corresponds to a S/W of ~ 0.67 in Fig. 7. The water content should, however, vary depending on the weather conditions and will be less during the dry season. Interestingly, if the main ion species in the pore water are assumed to be Na^+ and Cl^-, the EC corresponds to a concentration of ~ 5.0×10^{-4} M (Fig. 9), above which the particle diameter increases quickly, owing to coagulation (Fig. 8; i.e., the critical coagulation concentration; Van Olphen 1977). This suggests that the cohesive strength of the materials increases quickly if the water content decreases from the state described above. In this case, heavy rainfall due to Typhoon Jebi (on 4 September) as well as intermittent rainfall over a period of several weeks in the summer of 2018 likely saturated the slip surface. As discussed above, this might have reduced its cohesive strength, and facilitated destabilization by coseismic ground motion and high-mobility flow after failure.

Electrophoretic measurement also revealed that the PZC of allophane is at pH = ~ 6.0 and the absolute zeta potential value is much smaller than that of the slip

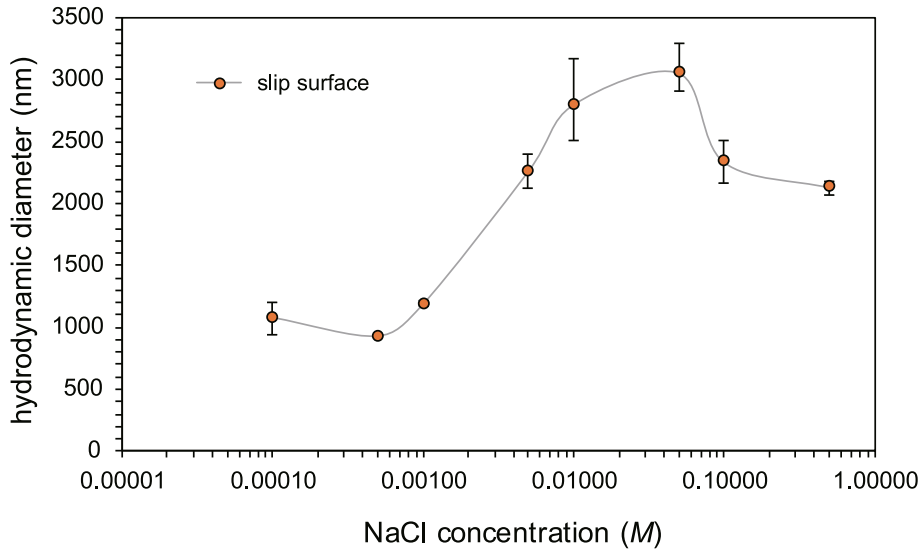

Fig. 9 Hydrodynamic diameter of particles (nm). The diameter was measured by dynamic light scattering as a function of solute concentration. Error bars denote the range of three repeated measurements

surface material at neutral pH (Fig. 8), suggesting that the cohesive strength of strata containing allophane is larger than those containing halloysite. This may be one reason why halloysite has often been observed in the slip surfaces of the landslides in volcanic areas (Chigira and Yokoyama 2005; Chigira et al. 2012; Nakano et al. 2013; Moon 2016; Kluger et al. 2017). In general, the alteration of volcaniclastic sediments first produces allophane, which is successively replaced by halloysite (Wada 1977, 1980; Parfitt et al. 1983), possibly due to dissolution–recrystallization transformation processes (Inoue 1996). Consequently, the main clay component varies with depth within volcanic soil deposits. According to Kameda et al. (2019), in the landslide scarp studied, the natural water content increased with depth. This may be due to the presence of smectite within the basement marine strata, which acts as an impermeable barrier to rain water. The fluid-saturated environment created by this barrier may have further promoted the halloysite-forming alteration reaction at the base of the volcanic soil. Compilation of the ages of volcaniclastic deposits in Japan and New Zealand (Okada et al. 1986; Lowe 1986; Inoue 1996) indicates that halloysite starts to form ~ 10^4 years after deposition, which is consistent with the age of the studied strata (9 ka for Ta-d). Therefore, progression of the weathering reaction is likely a key process for the production of mechanically weak layers that can easily collapse in volcanic areas, as observed in the present landslides. It should be noted that the physico-chemical properties of the mineral surface vary greatly depending on the type of mineral (Mitchell and Soga 2005). Therefore, the mechanism of sediment weakening that leads to slope instability in other geological environments needs to be considered in conjunction with the constituent phases and chemical environment within the slope-forming materials.

Note that these inferences remain qualitative, and further work is necessary for more quantitative discussion. For instance, rain water in Tomakomai city, 10 km away from Atsuma town, does have Na^+ and Cl^- as its main ions species, but their concentrations fluctuate (Shibata and Sakuma 1994). The presence of other cation (such as Ca^{2+}, Mg^{2+}, or K^+) and anion (including SO_4^{2-} and NO^{3-}) species can modify the surface physico-chemical properties of the halloysite particles. Rheological measurements of halloysite suspensions have demonstrated that the yield stress generally increases with decreasing pH (Theng and Wells 1995). This can be interpreted as a decrease in interparticle potential at lower pH (Fig. 8). However, the suspension's rheology shows complicated behavior depending on NaCl concentration as well as the morphology of the halloysite (Theng and Wells 1995). In situ soil monitoring would provide precise information about the way the water's ionic composition changes during rainfall. In addition, future work should consider the rheological properties of halloysite-bearing soil under variable chemical conditions.

5 Conclusions

The mineralogical and physico-chemical properties of the slip surface material from a landslide triggered by the 2018 Hokkaido Eastern Iburi earthquake were examined. This study reached the following conclusions.

(1) TEM observation revealed that halloysite in the slip surface exhibited irregular and occasionally

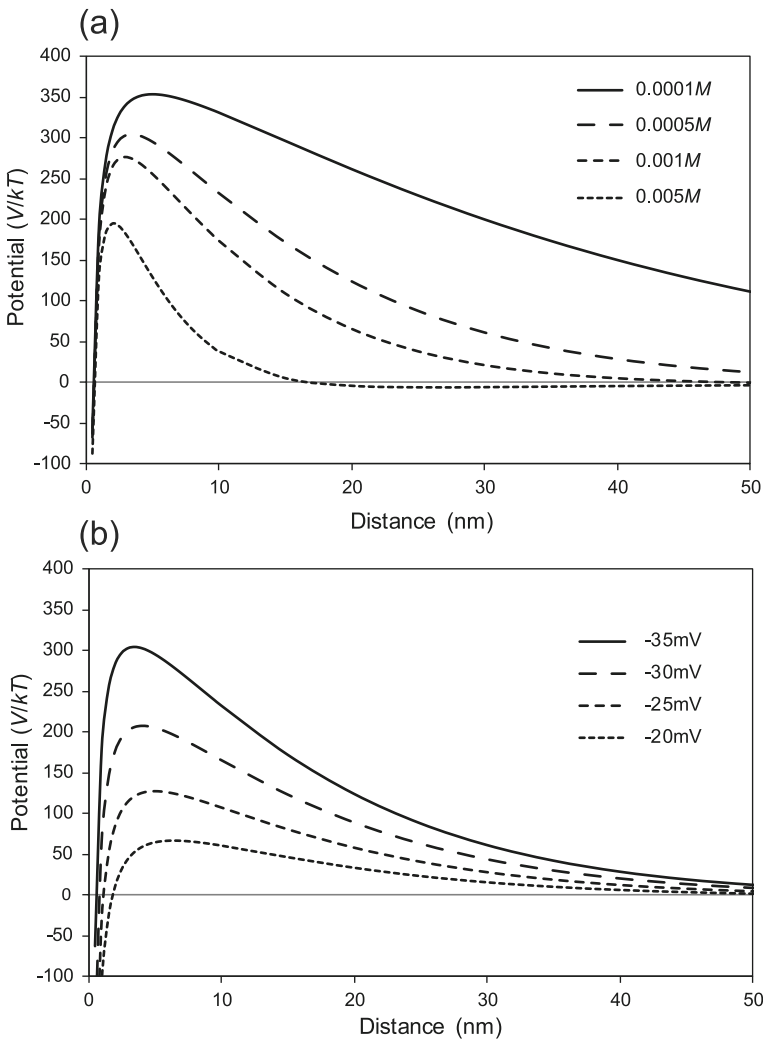

Fig. 10 Interparticle potential (in *kT*) based on DLVO theory. (a) The zeta potential was set at − 35 mV. (b) The solute concentration was set as 5.0×10^{-4} *M*

spherical morphology. Halloysite tubes or particles with a wood shaving-like shape, as documented in previous work, were not observed here.

(2) Halloysite in the slip surface has higher mesopore volumes than the reference tubular sample, which may be related to a high capacity of water retention after rainfall.

(3) To simulate possible chemical changes in soils during rainfall, samples were immersed in rainwater at different solid/water ratios. Increasing rainwater infiltration appeared to increase the pH and decrease the electrical conductivity within the slip surface.

(4) Electrophoretic measurements showed that the zeta potential of the slip surface material behaved similarly to a reference halloysite sample, but with differences at lower pH. Generally, the absolute zeta potential values increased with increasing pH and decreasing solute concentration.

(5) Applying Derjaguin–Landau–Verwey–Overbeeck theory to the obtained zeta potentials derived the interparticle potential of halloysite. The potential increased with decreasing solute concentration and increasing absolute zeta potential. These findings collectively suggest that rainwater saturation enhanced the colloidal stability of halloysite particles and resulted in the decrease in cohesive strength of the material. These physico-chemical effects might also have affected the rheological properties of the volcanic soil and led to the eventual collapse and downflow of debris triggered by seismic ground motion.

Abbreviations
PSD: Particle size distribution; EC: Electrical conductivity; S/W: Solid/water weight ratios

Acknowledgements
I thank Shuhei Shimoda and Tatsuhiro Sigyo for technical assistance with the TEM observations and water adsorption–desorption experiment. I also acknowledge two anonymous reviewers and editor Masahiro Chigira for their constructive comments, which greatly improved the manuscript. The JEM-2100F Jeol instrument is registered with the Open Facility system and managed by the Global Facility Center, Creative Research Institution, Hokkaido University.

Author's contributions
JK designed the study, carried out the experimental study, analyzed the data, and constructed the manuscript. The author read and approved the final manuscript.

Funding
This work was supported by a JSPS Grant-in-Aid for Scientific Research (18H0129508).

Availability of data and materials
The datasets supporting the conclusions of this article are included within the article.

Declarations

Competing interests
The author declares no competing interests.

Received: 18 November 2020 Accepted: 15 May 2021
Published online: 21 June 2021

References
Askenasy PE, Dixon JB, McKee TR (1973) Spheroidal Halloysite in a Guatemalan Soil. Soil Sci Soc Am Proc 37(5):799–803. https://doi.org/10.2136/sssaj1973.03615995003700050045x

Barrett EP, Joyner LG, Halenda PP (1951) The determination of pore volume and area distributions in porous substances. I. Computations from Nitrogen Isotherms. J Am Chem Soc 73:373–380

Brigatti MF, Galan E, Theng BKG (2006) Structures and mineralogy of clay minerals. In: Bergaya F, Theng BKG, Lagaly G (eds) Handbook of clay science. Elsevier, Amsterdam, pp 19–86. https://doi.org/10.1016/S1572-4352(05)01002-0

Chigira M, Nakasuji A, Fujiwara S, Sakagami M (2012) Catastrophic landslides of pyroclastics induced by the 2011 off the Pacific Coast of Tohoku Earthquake. pp 139–147 in: Earthquake-induced landslides, Proc. Int. Symp. Earthquake-Induced Landslides, Kiryu, Japan, Springer

Chigira M, Tajika J, Ishimaru S (2019) Landslides of pyroclastic fall deposits induced by the 2018 Eastern Iburi Earthquake with special reference to the weathering of pyroclastics. DPRI Annuals 62:348–356

Chigira M, Yokoyama O (2005) Weathering profile of non-welded ignimbrite and the water infiltration behavior within it in relation to the generation of shallow landslides. Eng Geol 78(3-4):187–207. https://doi.org/10.1016/j.enggeo.2004.12.008

Duran JDG, Ontiveros A, Delgado AV, Gonzalez-Caballero F (1998) Kinetics and interfacial interactions in the adhesion of colloidal calcium carbonate to glass in a packedbed. Appl Surf Sci 134(1):125–138. https://doi.org/10.1016/S0169-4332(98)00217-7

Earthquake and Volcano Hazards Observation and Research Program (2019) Annual report. http://www.eri.u-tokyo.ac.jp/YOTIKYO/r1seikahoukoku/r1_kadai_seika_small.pdf

Em Y, Stoporev A, Semenov A, Glotov A, Smirnova E, Villevald G, Vinokurov V, Manakov A, Lvov Y (2020) Methane hydrate formation in halloysite clay nanotubes. ACS Sustainable Chem Eng 8(21):7860–7868. https://doi.org/10.1021/acssuschemeng.0c00758

Furukawa R, Nakagawa M (2000) Geological map of Tarumae volcano. Geological Survey of Japan

Geospatial Information Authority of Japan (2018a) https://maps.gsi.go.jp/index_3d.html?z=17&lat=42.7503723926834&lon=141.91060960292816&pxsize=2048&ls=std%7C20180906hokkaido_atsuma_0906do&blend=0#&cpx=10.581&cpy=-70.126&cpz=35.866&cux=0.077&cuy=-0.304&cuz=0.950&ctx=0.000&cty=0.000&ctz=0.000&a=1&b=0&dd=0

Geospatial Information Authority of Japan (2018b) https://maps.gsi.go.jp/#12/42.770442/141.985660/&base=std&ls=std%7C20180906hokkaido_atsuma_0906do%7Cexperimental_anno&blend=0&disp=111&lcd=20180906hokkaid

Hillier S (2000) Accurate quantitative analysis of clay and other minerals in sandstones by XRD: comparison of a Rietveld and a reference intensity ratio (RIR) method and the importance of sample preparation. Clay Minerals 35(1):291–302. https://doi.org/10.1180/000985500546666

Inoue A (1996) Solution-mediated phase transformations of clay minerals. Journal of the Mineralogical Society of Japan 25(4):189–197. https://doi.org/10.2465/gkk1952.25.189

Israelachvili JN (2011) Intermolecular and Surface Forces. 3rd Edition, Academic Press, Cambridge

Ito Y, Yamazaki S, Kurahashi T (2020) Geological features of landslides caused by the 2018 Hokkaido Eastern Iburi Earthquake in Japan. Geological Society, London, Special Publications 501. https://doi.org/10.1144/SP501-2019-122

Iyoda F, Hayashi S, Arakawa S, John B, Okamoto M, Hayashi H, Yuan G (2012) Synthesis and adsorption characteristics of hollow spherical allophane nano–particles. Appl Clay Sci 56:77–83. https://doi.org/10.1016/j.clay.2011.11.025

Joussein E, Petit S, Churchman J, Theng B, Righ D, Delvaux B (2005) Halloysite clay minerals — a review. Clay Minerals 40:383–426

Kameda J, Kamiya H, Masumoto H, Morisaki T, Hiratsuka T, Inaoi C (2019) Fluidized landslides triggered by the liquefaction of subsurface volcanic deposits during the 2018 Iburi–Tobu earthquake, Hokkaido. Sci Rep 9(1):13119. https://doi.org/10.1038/s41598-019-48820-y

Kasai M, Yamada T (2019) Topographic effects on frequency-size distribution of landslides triggered by the Hokkaido Eastern Iburi Earthquake in 2018. Earth Planets Space 71(1):89. https://doi.org/10.1186/s40623-019-1069-8

Katsui Y (1959) On the Shikotsu pumice-fall deposit. Special reference to the activity just before the depression of the Shikotsu caldera. Bull Volcanol Soc Jpn 2:33–48

Kawachi T, Matsuura Y, Iyoda F, Arakawa S, Okamoto M (2013) Preparation and characterization of DNA/allophane composite hydrogels. Coll Surf B: Biointerfaces 112:429–434. https://doi.org/10.1016/j.colsurfb.2013.08.011

Kluger MO, Moon VG, Kreiter S, Lowe DJ, Churchman GJ, Hepp DA, Seibel D, Jorat ME, Mörz T (2017) A new attraction-detachment model for explaining flow sliding in clay-rich tephras. Geology 45(2):131–134. https://doi.org/10.1130/G38560.1

Lagaly G (2006) Colloid clay science. In: Bergaya F, Theng BKG, Lagaly G (eds) Handbook of Clay Science. Elsevier, Amsterdam, pp 247–260. https://doi.org/10.1016/S1572-4352(05)01005-6

Lowe DJ (1986) Controls on the rates of weathering and clay mineral genesis in airfall tephras: a review and New Zealand case study. In: Colman SM, Dethier DP (eds) Rates of chemical weathering of rocks and minerals. Academic Press, pp 265–330

Mitchell JK, Soga K (2005) Fundamentals of soil behavior, 3rd edn. Wiley, New York, pp 111–130

Moon V (2016) Halloysite behaving badly: geomechanics and slope behaviour of halloysite-rich soils. Clay Miner 51(3):517–528. https://doi.org/10.1180/claymin.2016.051.3.09

Nakagawa M, Amma-Miyasaka M, Miura D, Uesawa S (2018) Tephrastratigraphy in Ishikari Lowland, Southwestern Hokkaido: eruption history of the Shikotsu-Toya volcanic field. Jour Geol Soc Jpn 124(7):473–489. https://doi.org/10.5575/geosoc.2018.0038

Nakano M, Chigira M, Choun-Sian L (2013) Landslides of pumice fall deposits induced by the 2009 Padang earthquake and the formation of halloysite. Japan Geosci, Union Meeting, Chiba, Japan

Noro H (1986) Hexagonal platy halloysite in an altered tuff bed, Komaki city, Aichi prefecture, Central Japan. Clay Miner 21(3):401–415. https://doi.org/10.1180/claymin.1986.021.3.11

Noro H, Yamada K, Suzuki K (1981) An application of electron probe microanalysis for clay minerals. Kobutsugaku Zasshi 15:42–54 (in Japanese)

Okada K, Ossaka J, Matsui K, Suzuki M (1986) On the factors influencing the weathering of tephras in various parts of Japan. J Mineral Soc Jpn 17:25–33

Osanai N, Yamada T, Hayashi S, Kastura S, Furuichi T, Yanai S, Murakami Y, Miyazaki T, Tanioka Y, Takiguchi S, Miyazaki M (2019) Characteristics of landslides caused by the 2018 Hokkaido Eastern Iburi Earthquake. Landslides 16(8):1517–1528. https://doi.org/10.1007/s10346-019-01206-7

Parfitt RL, Russell M, Orbell GE (1983) Weathering sequence of soils from volcanic ash involving allophane and halloysite, New Zealand. Geoderma 29(1):41–57. https://doi.org/10.1016/0016-7061(83)90029-0

Plaza I, Ontiveros-Ortega A, Calero J, Romero C (2018) A new approach to triggering mechanism of volcano landslides based on zeta potential and surface free energy balance. Geomorph 301:1–9. https://doi.org/10.1016/j.geomorph.2017.10.009
Saeki K, Sakai M, Wada S (2010) DNA adsorption on synthetic and natural allophanes. Appl Clay Sci 50(4):493–497. https://doi.org/10.1016/j.clay.2010.09.015
Shibata H, Sakuma T (1994) Acid deposition at forest regions in North-Western part of Tomakomai. Jpn J Soil Sci J Plant Nutr 65:313–320
Sing KSW, Everett DH, Haul RAW, Moscou L, Peirotti RA, Rouquerol J (1985) IUPAC commission on colloid and surface chemistry including catalysis. Pure Appl Chem 57(4):603–619. https://doi.org/10.1351/pac198557040603
Smalley I, Ross CW, Whitton J (1980) Clays from New Zealand support the inactive particle theory of soil sensitivity. Nature 288:576–577. https://doi.org/10.1038/288576a0
Smoluchowski MV (1921) Handbook of electricity and magnetism, vol 366. Barth, Leipzig
Środoń JS, Drits VA, Mccarty DK, Hsieh JCC, Eberl DD (2001) Quantitative X-ray diffraction analysis of clay-bearing rocks from random preparations. Clays Clay Minerals 49(6):514–528. https://doi.org/10.1346/CCMN.2001.0490604
Suzuki M, Suzuki S, Maeda M, Tomura S, Mizota T (2001) Hydration rate of allophane and imogolite by hydration heat measurement using as heat exchange absorbents for lower temperature heat source and speedy drying desiccant. J Ceramic Soc Jpn 109(10):874–881. https://doi.org/10.2109/jcersj.109.1274_874
Theng BKG, Wells N (1995) The flow characteristics of halloysite suspensions. Clay Miner 30(2):99–106. https://doi.org/10.1180/claymin.1995.030.2.02
Tomura S, Maeda M, Inukai K, Ohashi F, Suzuki M, Shibasaki Y, Suzuki S (1997) Water vapor adsorption property of various clays and related materials for applications to humidity self-control materials. Clay Sci 10:195–203
Van Olphen H (1977) An introduction to clay colloid chemistry. Wiley, New York
Vergaro V, Abdullayev E, Lvov YM, Zeitoun A, Cingolani R, Rinaldi R, Leporatti S (2010) Cytocompatibility and uptake of halloysite clay nanotubes. Biomacromolecules 11(3):820–826. https://doi.org/10.1021/bm9014446
Wada K (1977) Minerals in soil environments. Soil Science Society of America. Madison, WI 603–38
Wada K (1980) Soils with variable charge. New Zealand Society of Soil Science, Lower Hutt, p 87
Wada K (1989) Allophane and imogolite, in Minerals in soil environments (2nd ed) Soil Science Society of America. SSSA Book Series 1:1051–1087
Wada K, Mizota C (1979) The Clay Science Society of Japan, p 42
Wang FR, Fan XM, Yunus AP, Subramanian SS, Alonso-Rodriguez A, Dai LX, Xu Q, Huang RQ (2019) Coseismic landslides triggered by the 2018 Hokkaido, Japan (Mw 6.6), earthquake: spatial distribution, controlling factors, and possible failure mechanism. Landslide 16:1551–1566. https://doi.org/10.1007/s10346-019-01187-7
Wang S, Du P, Yuan P, Liu Y, Song H, Zhou J, Deng L, Liu D (2020) Structural alterations of synthetic allophane under acidic conditions: implications for understanding the acidification of allophanic Andosols. Geoderma 376:114561. https://doi.org/10.1016/j.geoderma.2020.114561
Yamada S (1958) Studies on the history of volcanic eruptions of alluvium epoch in Hokkaido on the basis of depositional features of the pyroclastics. Monog Ass Geol Collab Jpn 8:1
Yamagishi H, Yamazaki F (2018) Landslides by the 2018 Hokkaido Iburi-Tobu Earthquake on September 6. Landslides 15(12):2521–2524. https://doi.org/10.1007/s10346-018-1092-z
Zhang S, Li R, Wang F, Lio A (2019) Characteristics of landslides triggered by the 2018 Hokkaido Eastern Iburi earthquake, Northern Japan. Landslides 16(9):1691–1708. https://doi.org/10.1007/s10346-019-01207-6

Publisher's Note